Tight constraints on the excess radio background at z = 9.1 from LOFAR

Mondal, R ; Fialkov, A ; Fling, C ; Iliev, I T ; Barkana, R ; Ciardi, B ; Mellema, G ; Zaroubi, S ; Koopmans, L V E ; Mertens, F G ; Gehlot, B K ; Ghara, R ; Ghosh, A ; Giri, S K ; Offringa, A ; Pandey, V N

Abstract: The ARCADE2 and LWA1 experiments have claimed an excess over the cosmic microwave background (CMB) at low radio frequencies. If the cosmological high-redshift contribution to this radio background is between 0.1 per cent and 22 per cent of the CMB at 1.42 GHz, it could explain the tentative EDGES low-band detection of the anomalously deep absorption in the 21-cm signal of neutral hydrogen. We use the upper limit on the 21-cm signal from the Epoch of Reionization (z = 9.1) based on 141 h of observations with LOFAR to evaluate the contribution of the high-redshift Universe to the detected radio background. Marginalizing over astrophysical properties of star-forming haloes, we find (at 95 per cent CL) that the cosmological radio background can be at most 9.6 per cent of the CMB at 1.42 GHz. This limit rules out strong contribution of the high-redshift Universe to the ARCADE2 and LWA1 measurements. Even though LOFAR places limit on the extra radio background, excess of 0.1–9.6 per cent over the CMB (at 1.42 GHz) is still allowed and could explain the EDGES low-band detection. We also constrain the thermal and ionization state of the gas at z = 9.1, and put limits on the properties of the first star-forming objects. We find that, in agreement with the limits from EDGES high-band data, LOFAR data constrain scenarios with inefficient X-ray sources, and cases where the Universe was ionized by stars in massive haloes only.

DOI: https://doi.org/10.1093/mnras/staa2422

Originally published at:
Mondal, R; Fialkov, A; Fling, C; Iliev, I T; Barkana, R; Ciardi, B; Mellema, G; Zaroubi, S; Koopmans, L V E; Mertens, F G; Gehlot, B K; Ghara, R; Ghosh, A; Giri, S K; Offringa, A; Pandey, V N (2020). Tight constraints on the excess radio background at z = 9.1 from LOFAR. Monthly Notices of the Royal Astronomical Society, 498(3):4178-4191.
DOI: https://doi.org/10.1093/mnras/staa2422

Monthly Notices of the ROYAL ASTRONOMICAL SOCIETY

MNRAS **498,** 4178–4191 (2020) doi:10.1093/mnras/staa2422
Advance Access publication 2020 September 2

Tight constraints on the excess radio background at $z = 9.1$ from LOFAR

R. Mondal [1,2★] A. Fialkov,[3★] C. Fling,[1] I. T. Iliev [1] R. Barkana,[4] B. Ciardi,[5] G. Mellema [2] S. Zaroubi,[6,7,8] L. V. E. Koopmans,[8] F. G. Mertens [8] B. K. Gehlot [9] R. Ghara [2,6,7] A. Ghosh [10] S. K. Giri [2,11] A. Offringa [12] and V. N. Pandey[8,12]

[1]*Astronomy Centre, Department of Physics and Astronomy, University of Sussex, Brighton BN1 9QH, UK*
[2]*The Oskar Klein Centre, Department of Astronomy, Stockholm University, AlbaNova, SE-10691 Stockholm, Sweden*
[3]*Institute of Astronomy, University of Cambridge, Madingley Road, Cambridge CB3 0HA, UK*
[4]*Raymond and Beverly Sackler School of Physics and Astronomy, Tel Aviv University, Tel Aviv 69978, Israel*
[5]*Max-Planck Institute for Astrophysics, Karl-Schwarzschild-Str. 1, D-85748 Garching, Germany*
[6]*Department of Natural Sciences, The Open University of Israel, 1 University Road, PO Box 808, Ra'anana 4353701, Israel*
[7]*Department of Physics, Technion, Haifa 32000, Israel*
[8]*Kapteyn Astronomical Institute, University of Groningen, PO Box 800, NL-9700 AV Groningen, the Netherlands*
[9]*School of Earth and Space Exploration, Arizona State University, 781 Terrace Mall, Tempe, AZ 85287, USA*
[10]*Department of Physics, Banwarilal Bhalotia College, Asansol, West Bengal 713303, India*
[11]*Institute for Computational Science, University of Zurich, Winterthurerstrasse 190, CH-8057 Zurich, Switzerland*
[12]*ASTRON – the Netherlands Institute for Radio Astronomy, Oude Hoogeveensedijk 4, NL-7991 PD Dwingeloo, the Netherlands*

Accepted 2020 August 7. Received 2020 July 20; in original form 2020 April 1

ABSTRACT

The ARCADE2 and LWA1 experiments have claimed an excess over the cosmic microwave background (CMB) at low radio frequencies. If the cosmological high-redshift contribution to this radio background is between 0.1 per cent and 22 per cent of the CMB at 1.42 GHz, it could explain the tentative EDGES low-band detection of the anomalously deep absorption in the 21-cm signal of neutral hydrogen. We use the upper limit on the 21-cm signal from the Epoch of Reionization ($z = 9.1$) based on 141 h of observations with LOFAR to evaluate the contribution of the high-redshift Universe to the detected radio background. Marginalizing over astrophysical properties of star-forming haloes, we find (at 95 per cent CL) that the cosmological radio background can be at most 9.6 per cent of the CMB at 1.42 GHz. This limit rules out strong contribution of the high-redshift Universe to the ARCADE2 and LWA1 measurements. Even though LOFAR places limit on the extra radio background, excess of 0.1–9.6 per cent over the CMB (at 1.42 GHz) is still allowed and could explain the EDGES low-band detection. We also constrain the thermal and ionization state of the gas at $z = 9.1$, and put limits on the properties of the first star-forming objects. We find that, in agreement with the limits from EDGES high-band data, LOFAR data constrain scenarios with inefficient X-ray sources, and cases where the Universe was ionized by stars in massive haloes only.

Key words: methods: statistical – dark ages, reionization, first stars – diffuse radiation – cosmology: theory.

1 INTRODUCTION

Studies of the Epoch of Reionization (EoR) and Cosmic Dawn are key to understanding early galaxy formation and the evolution of the intergalactic medium (IGM; see e.g. reviews by Barkana & Loeb 2001; Furlanetto, Oh & Briggs 2006; Barkana 2018a; Mesinger 2019). Ionizing properties of the high-redshift sources are currently largely constrained by the measurement of the electron scattering optical depth, τ, estimated by Planck (e.g. Planck Collaboration VI 2018), Ly α damping wing absorption in the spectra of the high-redshift quasars (e.g. Greig et al. 2017; Greig, Mesinger & Bañados 2019) and Ly α emission from Lyman Break galaxies (Mason et al. 2018). Accumulating evidence supports rapid and late reionization completed by $z \sim 6$ (e.g. Weinberger, Haehnelt & Kulkarni 2019), while galaxy surveys provide independent constraints on star formation out to $z \sim 10$ (e.g. see Behroozi et al. 2019, and references therein). However, these observations do not constrain properties of the first population of star-forming objects such as their star formation efficiency, feedback mechanisms that regulated primordial star formation, and the properties of the first sources of heat (e.g. X-ray binaries). These properties can be probed using low-frequency radio observations of the redshifted 21-cm signal of neutral hydrogen (e.g. Pober et al. 2014; Greig, Mesinger & Pober 2016; Singh et al. 2017; Monsalve et al. 2018, 2019).

The 21-cm signal is produced by atomic hydrogen in the IGM. The hyper-fine splitting of the lowest energy level of a hydrogen atom gives rise to the rest frame $\nu_{21} = 1.42$ GHz radio signal with the equivalent wavelength of about 21 cm (see Barkana 2018a; Mesinger 2019 for a recent review). Owing to its dependence on the underlying astrophysics and cosmology, this signal is a powerful tool to characterize the formation and the evolution of the first populations of astrophysical sources and, potentially, properties of dark matter, across cosmic time. Because the 21-cm signal is measured against the diffused radio background, usually assumed to be only the cosmic microwave background (CMB), this signal can also be used to

★ E-mail: rajesh@astro.su.se (RM); afialkov@ast.cam.ac.uk (AF)

constrain properties of any excess background radiation at low radio frequencies.

Recently, a detection of the global 21-cm signal from $z \sim 17$ was reported by the EDGES collaboration (Bowman et al. 2018). The reported signal significantly deviates from standard astrophysical models (e.g. Cohen et al. 2017, show a large set of viable 21-cm global signals varying astrophysical parameters in the broadest possible range) and concerns about the signal being of cosmological origin have, therefore, been expressed (Hills et al. 2018; Sims & Pober 2019; Singh & Subrahmanyan 2019; Bradley et al. 2019; Spinelli, Bernardi & Santos 2019). Despite these concerns, several theories have been proposed to explain the stronger than expected absorption, e.g. overcooling of hydrogen gas by dark matter (Barkana 2018b). Alternatively, the existence of a new component of radio background at low radio frequencies in addition to the CMB could also lead to a deeper 21-cm absorption feature due to the stronger contrast between the temperatures of the background and the gas (e.g. Bowman et al. 2018; Feng & Holder 2018). Astrophysical sources such as supernovae or accreting supermassive black holes (Biermann et al. 2014; Ewall-Wice et al. 2018; Ewall-Wice, Chang & Lazio 2019; Jana, Nath & Biermann 2019; Mirocha & Furlanetto 2019) could produce such an extra radio background. However, these sources would need to be several orders of magnitude more efficient in producing synchrotron radiation than corresponding sources at low redshifts (see Sharma 2018; Ewall-Wice et al. 2019), which is not very likely. An extra radio background can also be created by more exotic agents such as active neutrinos (Chianese et al. 2018), dark matter (Fraser et al. 2018; Pospelov et al. 2018), or superconducting cosmic strings (Brandenberger, Cyr & Schaeffer 2019). Interestingly, excess radio background at low radio frequencies was detected by the ARCADE2 collaboration at 3–90 GHz (Fixsen et al. 2011) as well as by LWA1 at 40–80 MHz (Dowell & Taylor 2018). Specifically, the latter measurement shows that the excess can be fitted by a power law with a spectral index of -2.58 ± 0.05 and a brightness temperature of 603^{+102}_{-92} mK at the reference frequency 1.42 GHz. However, the nature of this excess is still debated (Subrahmanyan & Cowsik 2013).

Apart from the EDGES low-band, several other global signal experiments report upper limits. At Cosmic Dawn, an upper limit of 890 mK on the amplitude of the 21-cm signal at $z \sim 20$ (Bernardi et al. 2016) was derived using the Large-Aperture Experiment to Detect the Dark Ages (LEDA; Price et al. 2018). At lower redshifts both the EDGES high-band collaboration ($z \sim 6.5$–14.8; Monsalve et al. 2017) and the Shaped Antenna measurement of the background RAdio Spectrum (SARAS2; $z \sim 6.1$–11.9; Singh et al. 2017) reported non-detection, which allowed to disfavour astrophysical scenarios with negligible X-ray heating. Using the same astrophysical modelling as we employ here,[1] the SARAS2 team ruled out 25 'cold' scenarios out of a set of 264 different signals compiled by Cohen et al. (2017) at greater than 5σ rejection significance (Singh et al. 2018); while Monsalve et al. (2019) placed 68 per cent limits on the X-ray heating efficiency of early sources and other astrophysical parameters using EDGES high-band data and 3.2 million models generated with the global signal emulator 21 cm GEM (Cohen et al. 2020).

In parallel, interferometric radio arrays are placing upper limits on the fluctuations of the 21-cm signal, including the Low-Frequency Array (LOFAR[2]; Patil et al. 2017; Gehlot et al. 2019; Mertens et al. 2020), the Murchison Widefield Array (MWA[3]; Beardsley et al. 2016; Barry et al. 2019; Li et al. 2019; Trott et al. 2020), the Donald C. Backer Precision Array for Probing the Epoch of Reionization (PAPER[4]; Kolopanis et al. 2019), the Giant Metrewave Radio Telescope (GMRT[5]; Paciga et al. 2013), and the Owens Valley Radio Observatory Long Wavelength Array (OVRO-LWA[6]; Eastwood et al. 2019).

The recently reported LOFAR measurements (Mertens et al. 2020) are based on 141 h of observations and are currently the tightest upper limits on the 21-cm power spectrum from $z = 9.1$, making it possible to rule out scenarios of cold IGM. Using these data, Ghara et al. (2020) find a lower limit of 3.55 K (95 per cent) on the gas temperatures at $z = 9.1$ in the case of their non-uniform scenario with the CMB as the background radiation (for reference, gas temperature in an adiabatically expanding universe without astrophysical sources of heating is 2.1 K at $z \sim 9.1$). In this paper, we use the LOFAR upper limits to constrain any excess radio background. We also derive limits on astrophysical parameters and the properties of the IGM with and without the excess radio contribution.

This paper is structured as follows. In Section 2, we describe the simulations used to generate the mock data sets of the 21-cm power spectra. In Section 3, we describe the mock data set and the ranges of parameters probed. In Section 4, we discuss the statistical analysis employed to constrain the model parameters. In Section 5, we report our constraints on the amplitude of the excess radio background and compare it to the values that could explain the EDGES low-band detection. We also place limits on the thermal and ionization state of the gas at $z = 9.1$, and on the properties of the first star-forming objects. We provide a qualitative comparison with the results of Ghara et al. (2020) in Section 6. Finally, we conclude in Section 7.

2 SIMULATED 21-CM SIGNAL

2.1 Theoretical modelling

The 21-cm signal of neutral hydrogen observed against a background radiation of the brightness temperature $T_{\rm rad}$ (at 1.42 GHz at redshift z) depends on the processes of cosmic heating and ionization. The brightness temperature of the 21-cm signal is given by

$$T_{21} = \frac{T_{\rm S} - T_{\rm rad}}{1+z}\left(1 - {\rm e}^{-\tau_{21}}\right), \quad (1)$$

where $T_{\rm S}$ is the spin temperature of the transition which at Cosmic-Dawn redshifts is coupled to the kinetic temperature of the gas, $T_{\rm gas}$, through Ly α photons produced by stellar sources (Wouthuysen 1952; Field 1958). The value of τ_{21} is the optical depth at redshift z given by

$$\tau_{21} = \frac{3h_{\rm pl}A_{10}c\lambda_{21}^2 n_{\rm H}}{32\pi k_B T_{\rm S}(1+z){\rm d}v/{\rm d}r}, \quad (2)$$

where ${\rm d}v/{\rm d}r = H(z)/(1+z)$ is the gradient of the line-of-sight component of the comoving velocity field, $H(z)$ is the Hubble rate at z, and $n_{\rm H}$ is the neutral hydrogen number density at z that depends on the ionization fraction and is driven by both ultraviolet and X-ray photons. The spin temperature encodes complex astrophysical

[1] Independent astrophysical constraints were obtained from the EDGES high-band data (Monsalve et al. 2018) using a different set of models generated with 21 cm FAST (Mesinger, Furlanetto & Cen 2011).

[2] http://www.lofar.org
[3] http://www.haystack.mit.edu/ast/arrays/mwa
[4] http://eor.berkeley.edu
[5] http://www.gmrt.ncra.tifr.res.in
[6] https://www.ovro.caltech.edu/

dependencies and can be written as

$$T_{\rm S} = \frac{1 + x_C + x_\alpha}{T_{\rm rad}^{-1} + (x_C + x_\alpha)\, T_{\rm gas}^{-1}}, \tag{3}$$

where x_C is the collisional coupling coefficient and x_α is the Wouthuysen–Field coupling coefficient (Wouthuysen 1952; Field 1958). Both x_C and x_α depend on the value of $T_{\rm rad}$:

$$x_\alpha = \frac{4P_\alpha}{27A_{10}} \frac{T_*}{T_{\rm rad}}, \tag{4}$$

with P_α being the total rate (per atom) at which Ly α photons are scattered within the gas and T_* is the effective temperature of the 21-cm transition (0.068 K). The collisional coupling coefficient is

$$x_C = \frac{n_i \kappa_{10}^i}{A_{10}} \frac{T_*}{T_{\rm rad}}, \tag{5}$$

where κ_{10}^i is the rate coefficient for spin de-excitation in collisions with the species of type i of density n_i, where we sum over species i (see e.g. Barkana 2016 for a recent review).

2.1.1 Radio background

Usually, the CMB is assumed to be sole contributor to the background radiation and $T_{\rm rad} = T_{\rm CMB}(1 + z)$, where $T_{\rm CMB}$ is the present-day value of the CMB temperature, 2.725 K. However, as was mentioned in Section 1, the anomalously strong EDGES low-band signal has encouraged the development of alternative models in which the radio background is enhanced (e.g. Bowman et al. 2018; Feng & Holder 2018). Here, we adopt a phenomenological global extra radio background with a synchrotron spectrum in agreement with observations by LWA1. The total radio background at redshift z is then given by

$$T_{\rm rad} = T_{\rm CMB}(1+z)\left[1 + A_{\rm r}\left(\frac{\nu_{\rm obs}}{78\ {\rm MHz}}\right)^{\beta}\right], \tag{6}$$

where $\nu_{\rm obs}$ is the observed frequency, $A_{\rm r}$ is the amplitude defined relative to the CMB temperature and calculated at the reference frequency of 78 MHz (which is the centre of the absorption trough reported by the EDGES collaboration) and $\beta = -2.6$ is the spectral index (in agreement with the LWA1 observation). We vary the value of $A_{\rm r}$ between 0 and 400 at 78 MHz with the upper limit being close to the LWA1 limit and corresponds to 21 per cent of the CMB at 1.42 GHz. All values of $A_{\rm r}$ between 1.9 (equivalent to 0.1 per cent of the CMB at 1.42 GHz) and 400 were shown to explain the EDGES low detection (for a tuned set of astrophysical parameters; see more details of the modelling in Fialkov & Barkana 2019).

2.1.2 Astrophysical parameters

Astrophysical processes affect the 21-cm signal by regulating the thermal and ionization states of the gas. In our modelling, we account for the effect of radiation (Ly α, Lyman–Werner, X-ray, and ionizing radiation) produced by stars and stellar remnants on the 21-cm signal (Visbal et al. 2012; Fialkov et al. 2013; Fialkov & Barkana 2014; Fialkov, Barkana & Visbal 2014; Cohen, Fialkov & Barkana 2016). The process of star formation is parametrized by two parameters. The first one is the value of circular velocity of dark matter haloes, V_c, which is varied between 4.2 km s^{-1} (molecular hydrogen cooling limit, corresponding to the dark matter mass of $M_{\rm h} = 1.5 \times 10^6$ M$_\odot$ at $z = 9.1$) and 100 km s^{-1} ($M_{\rm h} = 2 \times 10^{10}$ M$_\odot$ at $z = 9.1$). The high values of V_c implicitly take into account various chemical and mechanical feedback effects (e.g. the supernovae feedback which is expected to expel gas from small haloes thus rising the threshold mass for star formation), which we do not include explicitly. Cooling of gas via molecular hydrogen cooling channel, and subsequent star formation, happens in small haloes of circular velocity 4.2 km s^{-1} $< V_c <$ 16.5 km s^{-1} ($M_{\rm h} \sim 10^5$–10^7 M$_\odot$). Abundance of molecular hydrogen is suppressed by Lyman–Werner (LW) radiation (Haiman, Rees & Loeb 1997; Fialkov et al. 2013). Additional inhomogeneous suppression is introduced by the relative velocity between dark matter and baryons, $v_{\rm bc}$ (Tseliakhovich & Hirata 2010), which imprints the pattern of baryon acoustic oscillations (BAO) in the 21-cm signal (Dalal, Pen & Seljak 2010; Maio, Koopmans & Ciardi 2011; Visbal et al. 2012). Higher mass haloes ($V_c > 16.5$ km s^{-1}) form stars owing to atomic hydrogen cooling and are sensitive to neither the LW feedback nor to the effect of $v_{\rm bc}$, but are affected by photoheating feedback (Sobacchi & Mesinger 2013; Cohen et al. 2016; Sullivan, Iliev & Dixon 2018). The second parameter is the star formation efficiency, f_*, defined as the amount of gas in haloes that is converted into stars, which we vary in the range $f_* = 0.1$ per cent to 50 per cent. Star formation in molecular cooling haloes is assumed to be less efficient, which is implemented via a gradual low-mass cut-off (see Cohen et al. 2017 for more details). The broad considered range in the values of f_* is due to the lack of direct observations at high redshifts. Existing simulations of primordial star formation, although in general predict low values of f_*, show a large scatter in this parameter (e.g. Wise et al. 2014; O'Shea et al. 2015; Xu et al. 2016).

X-ray sources re-heat and mildly re-ionize the gas after the period of adiabatic cooling. Population synthesis simulations (Fragos et al. 2013) calibrated to low-redshift observations of X-ray binaries (e.g. Mineo, Gilfanov & Sunyaev 2012) suggest that high-mass X-ray binaries dominate the total X-ray budget at redshifts above $z \sim 6$. Here, we rely on this result and assume hard X-ray spectral energy distribution (SED) typical for a population of high-mass X-ray binaries at high redshifts (a complex function of X-ray energy with a peak at $\sim$2 keV adopted from Fragos et al. 2013). Another free parameter related to X-ray sources is the total X-ray luminosity, L_X. Observations of X-ray binaries in the local universe find a strong correlation between L_X and the star formation rate (e.g. Lehmer et al. 2010; Mineo et al. 2012). We adopt this dependence

$$L_X/{\rm SFR} = 3 \times 10^{40} f_X\ {\rm erg\ s^{-1} M_\odot^{-1}\ yr}, \tag{7}$$

introducing a normalization constant, f_X, which accounts for a possible change in X-ray efficiency at high redshifts. Here, we explore the wide range $f_X = 10^{-6}$–100. A value $f_X = 1$ yields L_X normalized to observations of X-ray binaries found in low-metallicity regions today (see Fragos et al. 2013, and references therein). Values of $f_X \gtrsim 100$ are unlikely (Fialkov et al. 2017) as such a population would saturate the unresolved X-ray background observed by the *Chandra* X-ray Observatory (Cappelluti et al. 2012; Lehmer et al. 2012), while values $f_X \lesssim 10^{-6}$ contribute negligible X-ray heating. We note that in this paper we ignore the ($\sim$ 10 per cent) effect of the CMB heating (Venumadhav et al. 2018) and the effect of Ly α heating (e.g. Chuzhoy & Shapiro 2007; Ghara & Mellema 2019).

In our simulations, the effects of ionizing radiation (ultraviolet radiation from stars) are defined by two parameters: the mean free path of ionizing photons, $R_{\rm mfp}$ = 10–70 comoving Mpc, and the ionizing efficiency of sources, ζ, which is tuned to yield the CMB optical depth τ in the range between 0.045 and 0.1. For a fixed set of astrophysical parameters, either ζ or τ can be used (for more details on the relation between ζ and τ, see Cohen et al. 2020). Here, we choose to use the latter as it is directly probed by the CMB experiments. The latest values of τ measured by the *Planck* satellite

Table 1. Summary of LOFAR measurements directly taken from table 4 of Mertens et al. (2020). From left to right: Central mode of each bin in units of $h\,\mathrm{Mpc}^{-1}$, the extent of each k bin, spherically averaged power spectrum in each bin, $1-\sigma$ error in the binned power spectrum.

k_c ($h\,\mathrm{Mpc}^{-1}$)	$k_1 - k_2$ ($h\,\mathrm{Mpc}^{-1}$)	Δ^2_{21} (mK^2)	$\Delta^2_{21,\,\mathrm{err}}$ (mK^2)
0.075	0.061−0.082	3476	916
0.100	0.082−0.111	9065	1155
0.133	0.111−0.150	20 211	1598
0.179	0.150−0.203	55 603	2684
0.238	0.203−0.274	128 842	4097
0.319	0.274−0.370	255 292	7727
0.432	0.370−0.500	441 200	12 778

are $\tau = 0.054 \pm 0.007$ (e.g. Planck Collaboration VI 2018). However, because in this paper we focus on the constraints at $z \sim 9$, we explore a broader range of values (0.045−0.1) including higher values of τ that can be constrained by the LOFAR data.

2.2 Simulation set-up

We use a hybrid computational framework[7] to estimate the evolution of the large scale 21-cm signal (Visbal et al. 2012; Fialkov & Barkana 2014; Fialkov et al. 2014; Cohen et al. 2017; Fialkov & Barkana 2019). The code takes into account all the physics specified in above. Processes on scales below the resolution scale of 3 comoving Mpc[8] (such as star formation, LW, and photoheating feedback effects, effects of v_{bc}) are implemented using sub-grid prescriptions. Radiation produced by stars and stellar remnants is propagated accounting for the effects of redshift on the energy of the photons and absorption in the IGM. Reionization is implemented using an excursion set formalism (Furlanetto, Zaldarriaga & Hernquist 2004). Astrophysical parameters (f_*, V_c, f_X, τ, R_{mfp}, A_r, and the SED of X-ray photons) are received as an input. The code generates cubes of the 21-cm signal at every redshift along with the temperature of the neutral IGM, ionization state, intensity of the Ly α, and LW backgrounds. The comoving volume of each simulation box is 384^3 Mpc^3. The simulation is run from $z = 60$ to $z = 6$.

We do not vary cosmological parameters with the exception of τ. The values of other cosmological parameters are fixed to the values reported by the *Planck* collaboration (Planck Collaboration XVI 2014).

3 MOCK DATA SETS AND PARAMETER SETS

Using the framework described in the previous section, we run a total of 23 972 simulations varying the astrophysical and background parameters in the ranges outlined above. A total of 7702 of these models have a boosted radio background with respect to the CMB and are referred to as the *excess-background* models, while the remainder are reference standard models with $A_r = 0$ (used as a separate data set). All these models were generated using the same set of initial conditions for the distribution and velocities of dark matter and baryons (the *fiducial* IC).

[7]Our code has similar architecture to the publicly available 21 cm FAST code of Mesinger et al. (2011), but the implementation is completely independent.
[8]The resolution of our simulation, 3 comoving Mpc, is motivated by the coherence scale of the relative velocity between dark matter and gas, v_{bc} (Tseliakhovich & Hirata 2010).

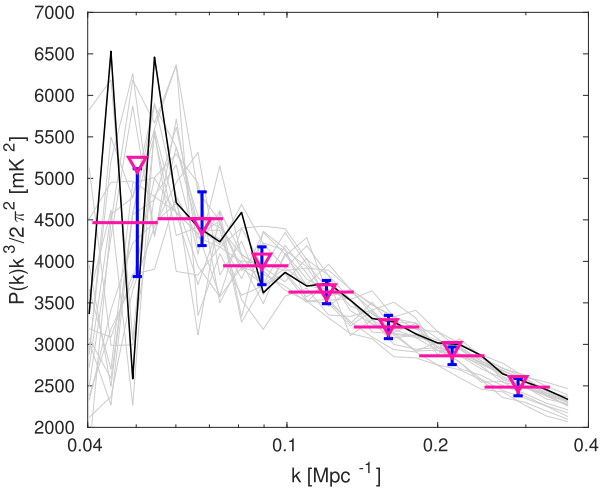

Figure 1. Simulated power spectrum as a function of the comoving wavenumber binned in redshift over the range $z = 8.7-9.6$. Solid black line is the result of a simulation with our fiducial set of initial conditions; grey lines are the results of 17 additional runs with other sets of initial conditions but same astrophysical and cosmological parameters ($f_* = 45$ per cent, $V_c = 100$ km s^{-1}, $R_{\mathrm{mfp}} = 55$ Mpc, $\tau = 0.0738$, $f_X = 10^{-4}$, $A_r = 0$). Triangles mark the binned power spectra for our fiducial IC in the seven LOFAR bins; magenta horizontal lines show the extent of each wavenumber bin; blue error bars are the $1-\sigma$ variation in the binned power spectrum calculated from 18 realizations of the initial conditions. For the selected astrophysical scenario the deviations of the binned power spectra calculated from the fiducial set of IC from the ensemble mean are 1.1σ, 0.19σ, 0.35σ, 0.17σ, 0.19σ, 0.9σ, and 0.6σ (listed from the lowest to the highest wavenumber). The corresponding values of b_{SV} (see the text) are 0.86, 1.01, 0.98, 0.99, 0.99, 0.97, 0.97, respectively.

For each simulation, we calculate the values of the spherically averaged binned 21-cm power spectra $P(k_c)$, where k_c is the centre of a wave-number bin chosen by Mertens et al. (2020). The power spectrum is averaged over redshifts $z = 8.7-9.6$ (to account for the LOFAR bandwidth), and binned over wave numbers in agreement with the LOFAR observational set-up (see Table 1 for the details of the wave-number binning). From each simulation, we also extract: the mean temperature of the gas in neutral regions at $z = 9.1$, T_{gas}, the mean ionization fraction at $z = 9.1$, $\bar{x}_{\mathrm{H\,II}}$, the redshift at which the ionization fraction (of volume) is 50 per cent, z_{re}, and the duration of reionization Δz, defined as the redshift range between the epoch when the mean ionization fraction was 90 per cent and 10 per cent.

3.1 Sample variance

The lowest wave number observed by Mertens et al. (2020) with LOFAR is $k_c = 0.075\,h\,\mathrm{Mpc}^{-1}$, which corresponds to the scale of ∼125 comoving Mpc and is a significant fraction of the size of our simulation box (384 Mpc). Therefore, power spectrum in the lowest k-bin is subject to statistical fluctuations due to *sample variance*, as is shown in Fig. 1. For the set of initial conditions that we used to generate the entire data set (our *fiducial* IC), the bin-averaged power spectrum in the lowest k-bin is 1.1σ away from the mean calculated over 18 realizations. We correct for this systematic offset by introducing a bias factor.

We perform an auxiliary suite of simulations to systematically estimate the effect of sample variance. For each set of astrophysical

parameters out of 360 selected combinations,[9] 10 simulations with different initial conditions, including the fiducial set, were performed. The bias in the binned power spectrum was subsequently calculated for every k-bin as the ratio of the binned power spectrum averaged over 10 realizations to the one derived from the fiducial set:

$$b_{\rm SV}(k_c) = \frac{\bar{P}(k_c)}{P_{\rm fiducial}(k_c)}. \tag{8}$$

We find that at $z = 9.1$ (close to the mid-point of reionization for the models that can be constrained by LOFAR in the standard case) the bias varies as a function of the reionization parameters τ and $R_{\rm mfp}$, while it has a very weak dependence on the rest of the parameters (V_c, f_*, f_X, and $A_{\rm r}$). We jointly fit the bias as a second-order polynomial in τ times a linear function of $R_{\rm mfp}$. Because the entire data set described in Section 3 was created using the fiducial IC set, we apply the corresponding parameter-dependent and k_c-dependent bias factor to all the simulated results to compensate for the effect of sample variance. Multiplying by the bias factor is essentially equivalent to averaging over 10 simulations.

Furthermore, we fit the variation in the simulated power in each bin ($\sigma_{\rm SV,\,sim}(k_c)$, blue error bars in Fig. 1), as a function of astrophysical parameters. We find that the fractional standard deviation, $\sigma_{\rm SV,\,sim}(k_c)/P_{\rm fiducial}(k_c)$, can be fitted with a quadratic function of τ times a linear function of $R_{\rm mfp}$, similarly to $b_{\rm SV}(k_c)$. The variation due to sample variance has a very weak dependence on V_c, f_*, f_X, and $A_{\rm r}$. The error in the power spectrum (after it has been corrected by the bias factor) is then given by $\sigma_{\rm SV,sim}(k_c)/\sqrt{10}$.

Finally, in order to account for theoretical uncertainty in modelling,[10] we impose a lower limit of 10 per cent on the relative error of the power spectrum of each individual simulation (Ghara et al. 2020). In the total error budget of the corrected power spectrum, this error should also be divided by $\sqrt{10}$.

The total theoretical parameter-dependent error in the binned power spectrum is, thus, given by

$$\sigma_{\rm th}(k_c) = \sqrt{\frac{\left[0.1 \times \Delta^2_{\rm th}(k_c)\right]^2 + \sigma^2_{\rm SV,sim}(k_c)}{10}}, \tag{9}$$

where $\Delta^2_{\rm th}(k_c) = P_{\rm fiducial}(k_c)k_c^3/\left(2\pi^2\right)$ is the calculated power spectrum in mK^2 units.

3.2 Binning over the model parameters

Our goal is to derive constraints on the excess radio background and also explore implications for the rest of the model parameters, as well as for the thermal and ionization states of the IGM. Based on the value of the power spectrum for each set of model parameters, we evaluate the likelihood of each point in the parameter space $\vec{\theta}$ as described in the next section. We, therefore, need to bin the parameter space $\vec{\theta}$ and calculate the binned power spectra $\Delta^2_{\rm th}(k_c, \vec{\theta})$ and the corresponding theoretical error $\sigma_{\rm th}(k_c, \vec{\theta})$. To remind the reader, $\Delta^2_{\rm th}(k_c, \vec{\theta})$ and $\sigma_{\rm th}(k_c, \vec{\theta})$ are binned in redshift, wave number, and $\vec{\theta}$.

We explore two distinct sets of the parameter spaces with $\vec{\theta}$ defined as either the model parameters $\vec{\theta} = [f_*,\ V_c,\ f_X,\ \tau,\ R_{\rm mfp},\ A_{\rm r}]$ or the derived IGM quantities $\vec{\theta} = [T_{\rm gas},\ \bar{x}_{\rm H\,II},\ z_{\rm re},\ \Delta z]$ that describe the state of the IGM. The range of each parameter is divided into 10 equally spaced bins, and each bin is tagged by the bin-averaged value of relevant parameters. Due to the large ranges, the binning is logarithmic for f_*, V_c, f_X, $A_{\rm r}$, and $T_{\rm gas}$, and linear for τ, $R_{\rm mfp}$, $\bar{x}_{\rm H\,II}$, $z_{\rm re}$, and Δz. We assume flat priors on each of the parameters across the entire allowed range (see Section 2): $0.001 \leq f_* \leq 0.5$, $4.2\ {\rm km\,s^{-1}} \leq V_c \leq 100\ {\rm km\,s^{-1}}$, $10^{-6} \leq f_X \leq 100$, $0.045 \leq \tau \leq 0.1$, $10 \leq R_{\rm mfp} \leq 70$ comoving Mpc and zero outside these ranges. In the standard case $A_{\rm r} = 0$ and in the excess background case, we vary $0.2 \leq A_{\rm r} \leq 400$ (thus covering the range 0.01–21 per cent of the CMB at 1.42 GHz). The priors on $[T_{\rm gas},\ \bar{x}_{\rm H\,II},\ z_{\rm re},\ \Delta z]$ are defined based on the ranges of these parameters found in our simulations: $2.2\ {\rm K} \leq T_{\rm gas} \leq 400\ {\rm K}$ (the lower limit is close to the temperature of the gas in an adiabatically expanding universe which is $\sim$2.1 K at $z = 9.1$), $0.02 \leq \bar{x}_{\rm H\,II} \leq 1.00$, $6 \leq z_{\rm re} \leq 10$ and $2 \leq \Delta z \leq 5$, and zero outside these ranges.

For $\vec{\theta} = [f_*,\ V_c,\ f_X,\ \tau,\ R_{\rm mfp},\ A_{\rm r}]$, this binning gives rise to 10^5 bins in the standard case and 10^6 bins in the excess-background case; for the IGM parameters $\vec{\theta} = [T_{\rm gas},\ \bar{x}_{\rm H\,II},\ z_{\rm re},\ \Delta z]$, there are 10^4 bins in each case. Due to the relatively small number of models, not all bins are populated. To solve this issue, we use the model sets to train artificial neural networks (ANN; see the Appendix for details) and use that to construct an emulator (similar approach has been taken by Kern et al. 2017; Cohen et al. 2019; Monsalve et al. 2019), which we then use to interpolate the empty bins.

4 STATISTICAL ANALYSIS METHODOLOGY

In general, the 21-cm signal is expected to be a non-Gaussian field (Bharadwaj & Pandey 2005; Mellema et al. 2006; Mondal et al. 2015) and the non-Gaussian effects will play a significant role in the error estimates of 21-cm power spectrum (Mondal, Bharadwaj & Majumdar 2016, 2017). In addition, the data in LOFAR bins are slightly correlated due to the finite station size. Therefore, the power-spectrum error-covariance matrix is expected to be non-diagonal. However, in reality bins show very weak correlation because the bins are chosen relatively wide compared to the footprint of an LOFAR station that acts as a spatial convolution kernel. With minimal error, we can therefore assume that the bins are uncorrelated and the covariance matrix is diagonal. The probability of a model (tagged by $\vec{\theta}$) given data can then be written as a product of the probabilities in each individual wavenumber bin $k_c \in k_i$. In addition, because of the bin-averaging and large-scales considered, we can assume that the signal is close to a Gaussian random field.

The LOFAR measurements reported by Mertens et al. (2020) are upper limits. Therefore, following Ghara et al. (2020), we can represent the probability of a model given the observed power-spectrum values using the error function:

$$\mathcal{L}(\vec{\theta}) = \prod_i \frac{1}{2}\left[1 + {\rm erf}\left\{\frac{\Delta^2_{21}(k_i) - \Delta^2_{\rm th}(k_i, \vec{\theta})}{\sqrt{2}\sigma(k_i, \vec{\theta})}\right\}\right], \tag{10}$$

where $\Delta^2_{21}(k_i)$ is the measured power spectrum in the ith k_c bin with uncertainty $\Delta^2_{21,\,\rm err}(k_i)$ listed in Table 1. The total variance in the bin is given by

$$\sigma(k_i, \vec{\theta}) = \sqrt{[\sigma_{\rm th}(k_i, \vec{\theta})]^2 + [\Delta^2_{21,\,\rm err}(k_i)]^2}. \tag{11}$$

According to this definition, the probability of a model is close to unity when its power spectrum at $z = 9.1$ is less than $[\Delta^2_{21}(k_i) -$

[9]The astrophysical parameters were selected such that the power spectra at $k_c = 0.075\,h\ {\rm Mpc}^{-1}$ are close to the LOFAR measurements by Mertens et al. (2020). This was done to ensure high precision in the testable range.

[10]The values of the 21-cm signal generated by the numerical simulation are subject to uncertainty. This is because some of the effects of order $\sim(1 + \delta)$, where δ is the stochastic dimensionless perturbation of the density field, have not been taken into account. For example, at the moment we assume linear growth of structure on large scales (>3 Mpc).

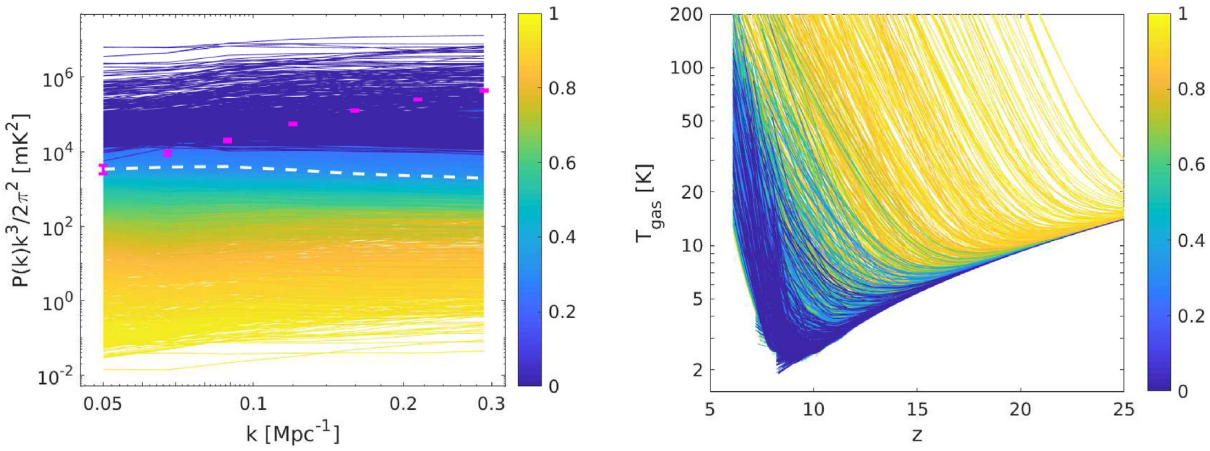

Figure 2. We show the excess-background models colour coded with respect to the probability that the data is consistent with the model (equation 10), as is indicated on the colour bar. Left: Binned power spectra versus wavenumber (in units of Mpc^{-1}, where we have assumed $h = 0.6704$ for conversion from Table 1) at $z = 9.1$. The white dashed line shows the maximum power of the models in the standard case (the corresponding likelihood value is $\mathcal{L} = 0.4898$). Magenta data points correspond to the LOFAR data from Table 1 (two-sided error bars). Right: corresponding thermal histories, i.e. evolution of the mean temperature of neutral intergalactic gas with redshift. Each curve is shown down to the (model-dependent) redshift of end of reionization.

$\sigma(k_i, \vec{\theta})]$ for all k_i, and the probability is close to zero when $\Delta^2_{\rm th}(k_i, \vec{\theta})$ is greater than $[\Delta^2_{21}(k_i) + \sigma(k_i, \vec{\theta})]$ for any k_i.

As an illustration, in Fig. 2 we show the complete set of excess-background power spectra (7702 models in total) colour coded by the probability that the data is consistent with the model. For comparison, we also show the maximum power of the models in the standard case (white line). The upper limits from Mertens et al. (2020) are plotted for reference. As we see from the figure, the current observational limits from LOFAR are strong enough to rule out a significant fraction of the explored excess-background scenarios (all corresponding to a cold IGM with ~ 50 per cent ionization at $z = 9.1$, as we will see later). However, for the standard astrophysical scenarios where the values of the power spectra are lower, only the most extreme models can be ruled out, and only in the lowest k-bin. A set of corresponding thermal histories is plotted in the right-hand panel of Fig. 2. The LOFAR upper limits by Mertens et al. (2020) disfavour a late X-ray heating that leaves the IGM cold for most of the EoR. Scenarios with early X-ray heating cannot be ruled out by the data as, typically, the corresponding power-spectrum values are low.

5 RESULTS

Using the predicted values of the spherically averaged binned power spectrum in all seven k-bins, we can rule out scenarios that yield strong fluctuations at $z = 9.1$. In the standard scenario with the CMB as a background radiation, a few factors need to come together to ensure maximum power. First, the spin temperature has to be fully coupled to the gas temperature, which, for realistic star formation scenarios, is guaranteed to be the case at $z = 9.1$ (e.g. Cohen, Fialkov & Barkana 2018). Secondly, the larger the contrast between $T_{\rm gas}$ and $T_{\rm rad}$, the stronger the signal. For $T_{\rm rad} = T_{\rm CMB}$, the strongest contrast between the two temperatures is reached in cases of cold IGM. In the case of the excess-background models, the coupling is less efficient compared to the standard models; however, the signals are enhanced due to the larger contrast between the gas temperature and the temperature of the background radiation. Similarly to the standard case, the deepest signals correspond to the scenarios with the inefficient X-ray heating. Finally, fluctuations in the gas temperature and the neutral fraction play a role. Because here we have chosen a hard X-ray spectrum (Fragos et al. 2013; Fialkov et al. 2014), heating is nearly homogeneous, and the dominant source of fluctuations at $z = 9.1$ is the non-uniform process of reionization with peak power at ~ 50 per cent ionization fraction. For a fixed thermal history, nearly homogeneous reionization would result in a smoother signal and, thus, lower power of the 21-cm fluctuations, compared to a patchy reionization scenario.

5.1 Limits on the excess-radio background

Using $\mathcal{L}(\vec{\theta})$, we calculate the normalized probability for each of the parameters, $\vec{\theta} = [f_*,\ V_c,\ f_X,\ \tau,\ R_{\rm mfp},\ A_{\rm r}]$, and parameter pairs, marginalizing over the rest of the parameter space. The resulting probability distributions are normalized using the criterion that the total probability (area under the curve) is 1 within the considered prior ranges. The resulting two-dimensional (2D) and one-dimensional (1D) probabilities of all the model parameters are shown in Fig. 3, where we divided each probability function by its peak value to show the marginalized likelihood of all possible combinations uniformly. Using 1D probabilities, we find the 68 per cent, 95 per cent, and 99 per cent confidence intervals for $A_{\rm r}$, and 68 per cent and 95 per cent confidence intervals for f_X, while the constraints on the other parameters are weaker and could be inferred only at 68 per cent level (see Table 2). We calculate each confidence level (CL) by selecting parameter-bins with the highest probability up to the corresponding cumulative probability (e.g. of 0.68 for the 68 per cent CL). We also note the limits where the 1D probabilities are below $\exp(-1/2)$ of the peak (similar to the Gaussian 1σ definition).

Marginalizing over the residual model parameters (f_*, V_c, f_X, τ, $R_{\rm mfp}$), we derive constraints on $A_{\rm r}$ finding that LOFAR upper limit rules out $A_{\rm r} > 15.9$ at 68 per cent, $A_{\rm r} > 182$ at 95 per cent and $A_{\rm r} > 259$ at 99 per cent, equivalent to 0.8 per cent, 9.6 per cent, and 13.6 per cent, respectively, of the CMB at 1.42 GHz. The 95 per cent limit on $A_{\rm r}$ of 182 is equivalent to 262 mK at 1.42 GHz and is within 3σ of the LWA1 measurement. The likelihood, which peaks at low values of $A_{\rm r}$, drops by a factor of $\exp(-1/2)$ by $A_{\rm r} = 60.9$ corresponding to 3.2 per cent of the CMB at 1.42 GHz. In our analysis, we have fixed the value of the spectral index of the radio background to $\beta = -2.6$. We have checked that the uncertainty

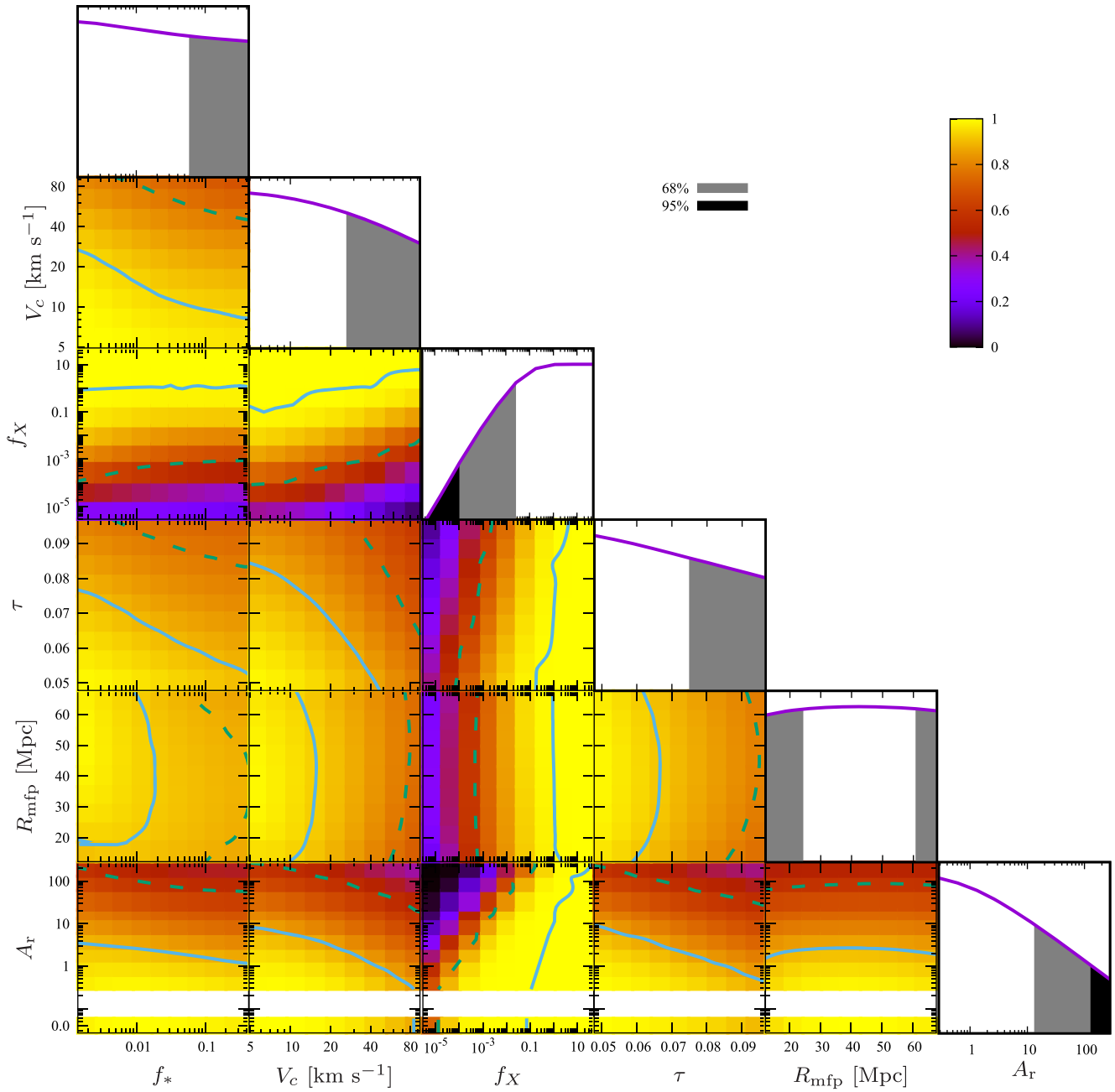

Figure 3. 1D and 2D marginalized likelihood of the astrophysical parameters (f_*, V_c, f_X, τ, $R_{\rm mfp}$, A_r) obtained using excess-background models. In addition, we append the normalized likelihood values for our standard models below the white band of the bottom row to highlight the consistency with the excess-background case. The standard-case normalized likelihood was calculated by using a joined set of the excess-background models and standard models. Regions of 2D marginalized likelihoods that are on the darker side (red, purple, and black) of the solid lines are disfavoured with more than 39 per cent (1σ in 2D) confidence, and the regions that are on the darker side of the dashed lines are disfavoured with more than 86 per cent (2σ in 2D) confidence. The grey regions in the 1D likelihood distribution are also disfavoured at the 68 per cent confidence level, and the black regions are disfavoured at the 95 per cent confidence level. We do not show the 99 per cent CL for $A_{\rm r}$ here, as it is close to the upper limits on the prior (set by the LWA1 limit). All limits are listed in Table 2.

in the spectral index $\Delta\beta = 0.05$, reported by LWA1 (Dowell & Taylor 2018), would lead to only up to ∼3 per cent variation in the intensity of the excess radio background at the frequency of 140 MHz corresponding to $z = 9.1$.

Fialkov & Barkana (2019) showed that the global signal reported by EDGES low band can be produced by adding an extra radio background with $1.9 < A_{\rm r} < 418$ relative to the CMB at the 78 MHz reference frequency (corresponding to 0.1−22 per cent of the CMB at 1.42 GHz). Even though part of this range is now ruled out by the new LOFAR limits, models with values of $A_{\rm r}$ between 0.1 per cent and 9.6 per cent (at 95 per cent CL) of the CMB at 1.42 GHz are still allowed and could fit the EDGES low-band detection. Such a small contribution is within the measurement error of LWA1 (Dowell & Taylor 2018, report excess background of 603^{+102}_{-92} mK at the 21-cm rest-frame frequency of 1.42 GHz) and would remain a plausible explanation for the detected EDGES signal even if the excess measured by ARCADE2 and LWA1 is due to an erroneous Galactic modelling (Subrahmanyan & Cowsik 2013).

Table 2. Limits on astrophysical parameters and the derived IGM parameters. From left to right: type of model and constraint; mean temperature of neutral gas at $z = 9.1$ in K; ionization fraction of the IGM; duration of reionization defined as the redshift interval between 90 per cent neutral IGM and 10 per cent neutral; redshift of the mid-point of reionization (defined as the redshift at which neutral fraction is 50 per cent); star formation efficiency; minimum circular velocity of star-forming haloes in km s^{-1}; X-ray heating efficiency; CMB optical depth; mean free path of ionizing photons in comoving Mpc; amplitude of the excess radio background compared to the CMB at the reference frequency of 78 MHz (as defined in equation 6). For the case of excess radio background (Ex. bck. in the table), we show both 68 per cent limits (top row), 95 per cent limits (second row) and 99 per cent limits (third row). We also find the parameter values at which the likelihood drops to exp(−1/2) of the peak value (third row). In the standard case, we can only show the 68 per cent limits, as the 1D PDFs are rather flat.

Model	$T_{\rm gas}$	$\bar{x}_{\rm H\,II}$	Δz	$z_{\rm re}$	f_*	V_c	f_X	τ	$R_{\rm mfp}$	$A_{\rm r}$
Ex. bck., 68 per cent	>16.1	< 38 per cent or > 72 per cent	>3	<8.21	<0.05	<28	$>1 \times 10^{-2}$	<0.076	>24 and <60	<15.9
Ex. bck., 95 per cent	>2.89	NA	NA	NA	NA	NA	$>1 \times 10^{-4}$	NA	NA	<182
Ex. bck., 99 per cent	>2.25	NA	NA	NA	NA	NA	NA	NA	NA	<259
Ex. bck., $e^{-1/2}$	>6.0	NA	NA	NA	NA	NA	$>8 \times 10^{-4}$	NA	NA	<60.9
Standard, 68 per cent	>10.1	< 38 per cent or > 72 per cent	>3	<8.51	<0.05	<36	$>5 \times 10^{-3}$	<0.080	<30 or >49	NA

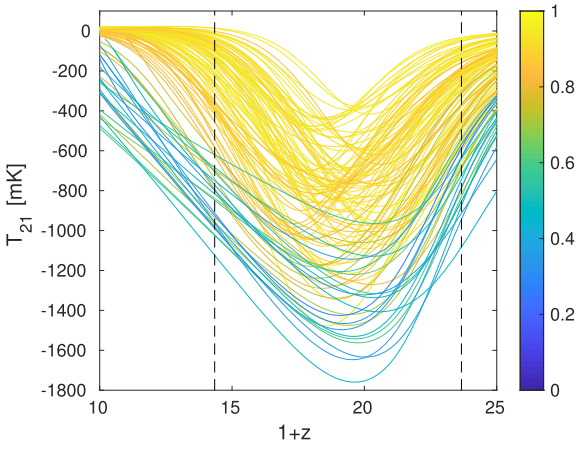

Figure 4. Excess-background global signals that are consistent with EDGES low-band, colour coded with respect to their model likelihood values under LOFAR (Equation 10) as is indicated on the colour bar. Vertical dashed lines mark the frequency range of 60–99 MHz over which the best-fitting detected signal was reported (Bowman et al. 2018).

In Fig. 4, as an illustration, we show global 21-cm signals for those excess-background models from our data set that are broadly consistent with the tentative EDGES low-band detection. In order to define this consistency, we follow the simple approach taken by Fialkov & Barkana (2019) by requiring the signal to be deep, and localized within the band of the EDGES low instrument. Within 99 per cent confidence, the cosmological signal should satisfy

$$300\,{\rm mK} < \left\{\max\left[{\rm T}_{21}(60 < \nu < 68)\right] - \min\left[{\rm T}_{21}(68 < \nu < 88)\right]\right\} < 1\,{\rm K}, \quad (12)$$

and

$$300\,{\rm mK} < \left\{\max\left[{\rm T}_{21}(88 < \nu < 96)\right] - \min\left[{\rm T}_{21}(68 < \nu < 88)\right]\right\} < 1\,{\rm K}. \quad (13)$$

The signals in Fig. 4 are colour coded with respect to the LOFAR likelihood (same as in Fig. 2). All the signals consistent with EDGES low-band have relatively high LOFAR likelihood, $\mathcal{L} \geq 0.31$. This is because the EDGES detection implies an early onset of the Ly α coupling (Schauer, Liu & Bromm 2019) due to efficient star formation ($f_* > 2.8$ per cent) in lower-mass haloes with circular velocity below $V_c = 45\,{\rm km\,s^{-1}}$ (corresponding to $M_h < 7.8 \times 10^8\,{\rm M}_\odot$ at $z = 17$, Fialkov & Barkana 2019). In such models the IGM is heated and partially ionized by $z = 9.1$, resulting in relatively low-intensity 21-cm signals in the LOFAR band.

5.2 Astrophysical limits

Next, we explore the implications of the LOFAR upper limits for the rest of the model parameters (f_*, V_c, f_X, τ, $R_{\rm mfp}$). In this work, we assume hierarchical structure formation with a simple prescription for the formation of stars and X-ray binaries. Therefore, LOFAR limits at $z = 9.1$ can be used to constrain properties of the first star forming haloes (appearing at $z \sim 30$–60 in our simulations) and first sources of light at Cosmic Dawn. The resulting 2D and 1D probabilities are shown in Fig. 3 and the limits are summarized in Table 2. In the limiting case of the negligible radio background, our results converge to the standard case with the CMB as the background radiation. This trend is demonstrated in Fig. 3, where the 2D probabilities of standard models, with $A_{\rm r} = 0$, are appended below the white band. For completeness, we also explore the set of standard models separately, showing their 2D and 1D probabilities in Fig. 5 and listing the corresponding 68 per cent limits in Table 2.

All disfavoured models feature efficient star formation with $f_* \gtrsim 5$ per cent at 68 per cent CL (Table 2). However, the corresponding 1D marginalized likelihood is rather flat and never drops below a factor of exp(−1/2) relatively to its peak value. Higher values of f_* result in stronger fluctuations that are easier to rule out. Higher values of f_* also imply stronger Ly α background and, thus, an earlier onset of Ly α coupling that yields signals with larger amplitudes (e.g. Cohen et al. 2020).

Another model parameter related to star formation in first haloes is V_c. Higher V_c is equivalent to larger minimum mass of star-forming haloes that are more strongly clustered, thus yielding stronger fluctuations. In the hierarchical model of star formation that we adopt here, higher V_c also implies later onset of star formation and X-ray heating. In such models, chances are that fluctuations (e.g. heating) are not yet saturated by $z = 9.1$ resulting in stronger 21-cm signals that can be ruled out by LOFAR. We find that values of V_c above $28\,{\rm km\,s^{-1}}$ (corresponding to $4.5 \times 10^8\,{\rm M}_\odot$ at $z = 9.1$) are disfavoured by the data at 68 per cent (the corresponding 1D marginalized likelihood is rather flat and never drops below the threshold value of exp(− 1/2) relatively to its peak value). The standard-physics limit is $36\,{\rm km\,s^{-1}}$, or 9.5×10^8 M$_\odot$ at $z = 9.1$. Even though the limits on V_c are weak at the moment, the LOFAR

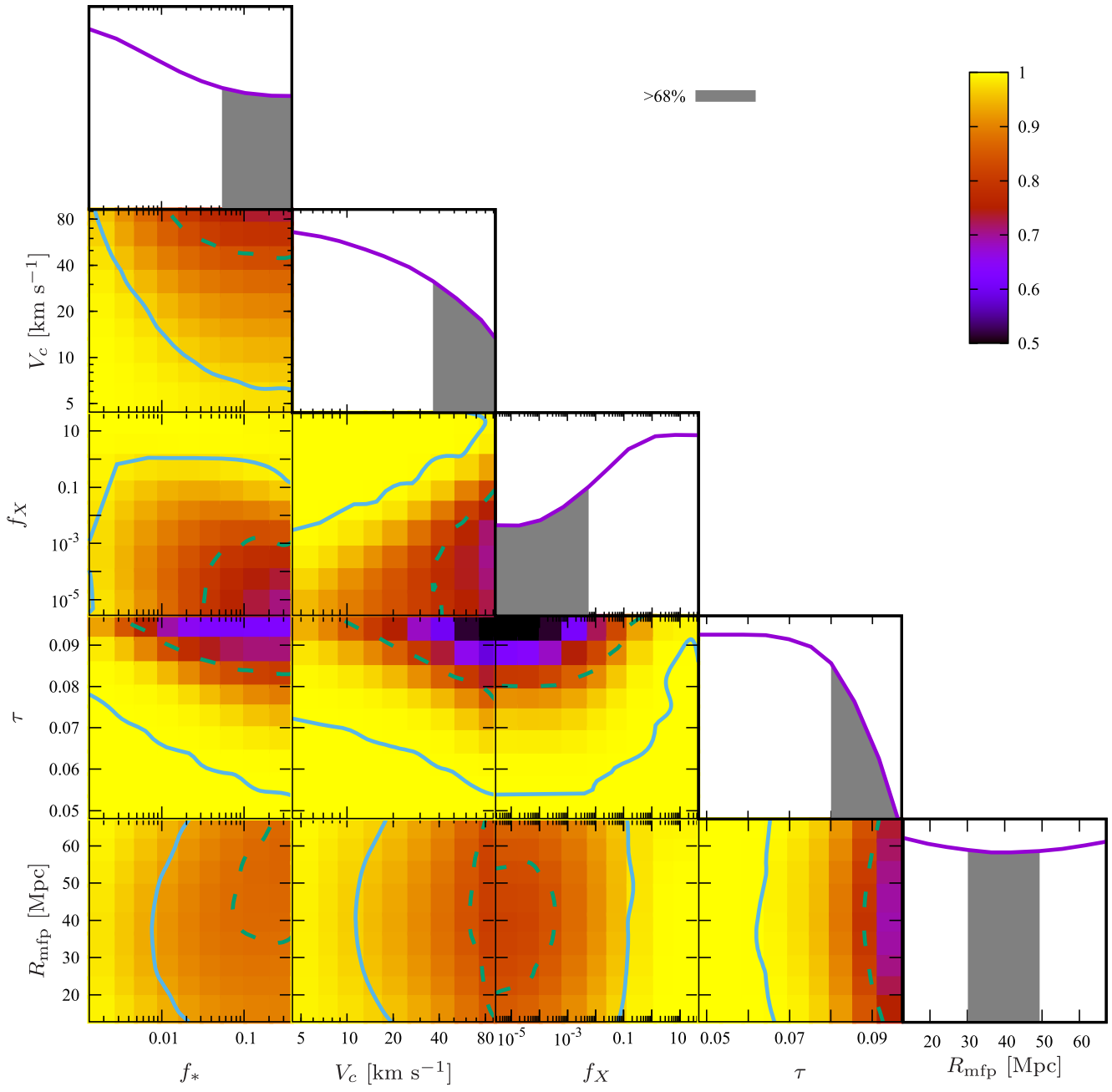

Figure 5. 1D and 2D marginalized likelihood of the astrophysical parameters (f_*, V_c, f_X, τ, $R_{\rm mfp}$) obtained using standard models ($A_{\rm r} = 0$). The regions of 2D marginalized likelihoods that are on the darker side of the solid lines are disfavoured with more than 39 per cent (1σ in 2D) confidence, and the regions that are on the darker side of the dashed lines are disfavoured with more than 86 per cent (2σ in 2D) confidence. The grey regions in the 1D likelihood distribution are also disfavoured at the 68 per cent confidence level (also listed in Table 2). Note that the colour scale is not the same as that in Fig. 3.

data favour the existence of low-mass haloes (in agreement with EDGES high-band results; Monsalve et al. 2019).

In our models, gas temperature is regulated by the interplay between several cooling and heating mechanisms with the major roles played by adiabatic cooling due to the expansion of the universe and X-ray heating by X-ray binaries, although the latter is partially degenerate with f_* and V_c that regulate the number of X-ray binaries.[11] Therefore, the X-ray efficiency of the first X-ray binaries is directly constrained by LOFAR with a values $f_X < 1 \times 10^{-2}$ disfavoured at 68 per cent CL and $f_X < 1 \times 10^{-4}$ disfavoured at 95 per cent CL, implying a lower limit on the total X-ray luminosity per star formation rate (equation 7) of 3×10^{38} erg s^{-1}M$_\odot^{-1}$ yr and 3×10^{36} erg s^{-1}M$_\odot^{-1}$ yr, respectively. The 1D likelihood, which peaks at high f_X values, is steep enough and drops below the threshold $\exp(-1/2)$ of its peak value at $f_X = 8 \times 10^{-4}$ (corresponding to 2.4×10^{37} erg s^{-1}M$_\odot^{-1}$ yr). In the standard case, only the 68 per cent limit can be calculated and is $f_X < 5 \times 10^{-3}$ (1.5×10^{38} erg s^{-1}M$_\odot^{-1}$ yr, respectively).

[11] The degeneracy is visible in the 2D PDFs of $f_* - f_X$ and $V_c - f_X$ shown in Figs 3 and 5.

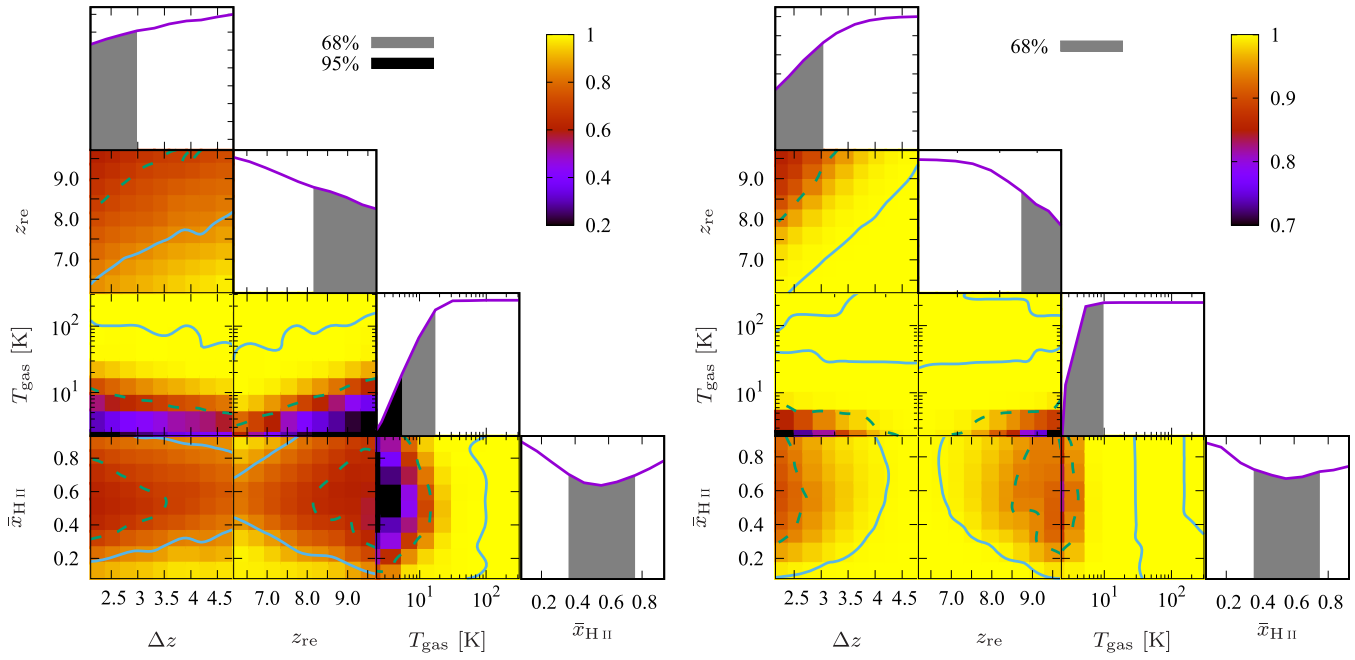

Figure 6. 1D and 2D marginalized likelihood of the IGM parameters [$T_{\rm gas}$, $\bar{x}_{\rm H\,II}$, Δz, z_{re}] obtained using excess-background models (left) and standard models (right). Note separate colour bars (top right of each panel). The regions of 2D marginalized likelihoods which are on the darker side of the solid lines are disfavoured with more than 39 per cent (1σ in 2D) confidence, and the region which is on the darker side of the dashed line is disfavoured with more than 86 per cent (2-σ in 2D) confidence. The grey regions in the 1D likelihood distribution are also disfavoured at the 68 per cent confidence level, and (for excess-background models) the black region is disfavoured with more than 95 per cent CL. The limits are listed in Table 2. Note that the colour scales are not the same as those in Figs 3 and 5.

The current LOFAR data also disfavour models with mid-point of reionization at $z \sim 9$. In such models the peak-power from ionizing fluctuations falls within the currently analysed LOFAR band, and, consequently, such models are relatively easy to exclude. This constraint can be mapped on to limits on τ: scenarios with $\tau > 0.076$ (excess background) or $\tau > 0.080$ (standard models) are disfavoured at 68 per cent. In both theories, the 1D likelihood curves of τ peak at low values of τ but do not drop below the threshold value of $\exp(-1/2)$ within the prior ranges. Finally, we find that the constraints on the model parameter $R_{\rm mfp}$ are very weak, with the 1D marginalized likelihood being very flat. This means that our model power spectrum is not sensitive to the changes in $R_{\rm mfp}$ value at $z \sim 9$.

5.2.1 *Comparison with EDGES*

Focusing on the standard models, we can compare the LOFAR limits reported above to the limits extracted from the data of the global 21-cm instrument EDGES high-band (90–190 MHz, correspond to the 21-cm signal from $z = 6-15$). Using a similar set of standard models and similar prior ranges of parameters as we explore here, Monsalve et al. (2019) found that the EDGES high-band data favour (at 68 per cent confidence) the following parameter ranges assuming a fixed X-ray SED (softer than what we use here; however, the global signal constraints prove to be nearly insensitive to the X-ray SED, Monsalve et al. 2019): $R_{\rm mfp} < 36.1$ Mpc, $V_c < 21.5\,{\rm km\,s^{-1}}$ (equivalent to $2 \times 10^8\,{\rm M}_\odot$ at $z = 9.1$), $f_X > 2.5 \times 10^{-3}$, $f_* < 0.4$ per cent or $f_* > 3.6$ per cent (signals with both lower and higher values of f_* are likely to be outside of the band of EDGES High), $\tau < 0.072$ or $0.074 < \tau < 0.079$ (where the second band is most likely due to the instrumental systematic). Overall, LOFAR and the EDGES high-band experiment are in agreement ruling out scenarios with inefficient X-ray heating and models in which the Universe was ionized by massive haloes only (of mass few $\times 10^8$ M$_\odot$ or higher, at $z \sim 9.1$). Similar trends were found with the SARAS2 data (although only 264 models were examined in that case; Singh et al. 2017).

5.3 Limits on the thermal and reionization histories

We use the LOFAR upper limits on the 21-cm power spectrum to put limits on the thermal and ionization state of the IGM at $z = 9.1$. We repeat the likelihood calculation applying it to the IGM parameters $\vec{\theta} = [T_{\rm gas},\ \bar{x}_{\rm H\,II},\ z_{\rm re},\ \Delta z]$. The resulting 2D and 1D probabilities of $T_{\rm gas}$, $\bar{x}_{\rm H\,II}$, $z_{\rm re}$, and Δz are shown in Fig. 6 (left-hand panel shows the case of the extra radio background, while the standard case is shown on the right for comparison). Our results are also summarized in Table 2. We have also tabulated the limits obtained from the regions where the 1D probabilities are below $\exp(-1/2)$ of the peak.

As we see from the figure and the table, the LOFAR data indeed disfavour scenarios with cold IGM. The lower limit on the temperature of neutral gas at $z = 9.1$ is 16.1 K at 68 per cent CL (while it is only 10.1 K in the standard case) 2.89 K at 95 per cent CL and 2.25 K at 99 per cent CL. The likelihood, which peaks at high values of $T_{\rm gas}$, drops by a factor of $\exp(-1/2)$ at $T_{\rm gas} = 6$ K in the excess-background case. As expected, there is some degree of degeneracy between the constraints on the thermal and reionization histories with the strongest limits on temperature coming from the cases with mid-point of reionization occurring at $z \sim 9$.

Through marginalizing over the thermal histories we can put limits on the process of reionization (Fig. 6 and Table 2). We find that the LOFAR limits disfavour fast reionization scenarios (with $\Delta z \lesssim 3$) with ionized fractions between $\sim$ 38 per cent and $\sim$72 per cent at $z =$

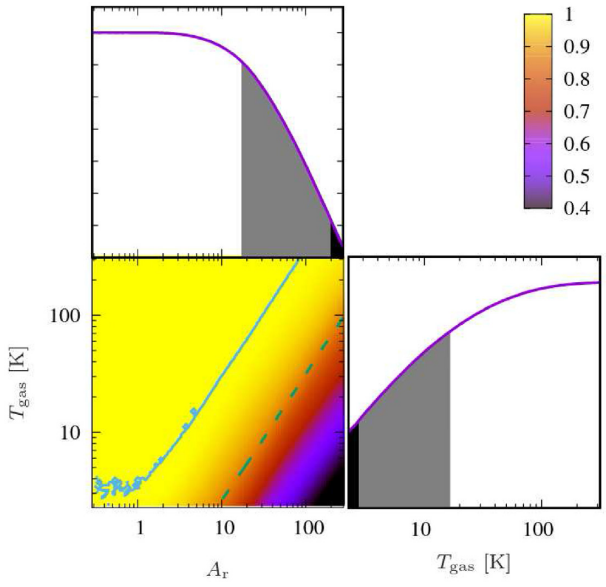

Figure 7. The optimal exclusion space of LOFAR: 1D and 2D marginalized likelihood of the excess-radio background parameter $A_{\rm r}$ and the IGM temperature $T_{\rm gas}$ obtained using excess-background models. The region of 2D marginalized likelihood which is on the darker side of the solid lines is disfavoured with more than 39 per cent (1σ in 2D) confidence, and the region which is on the darker side of the dashed line is disfavoured with more than 86 per cent (2σ in 2D) confidence. The grey regions in the 1D likelihood distributions are also disfavoured at the 68 per cent confidence level, and the black regions are disfavoured at the 95 per cent confidence level. To produce this figure, we have marginalized over V_c, f_X, and f_* and assumed fixed values of $R_{\rm mfp} = 40$ comoving Mpc and $\tau = 0.055$.

9.1. The high end of the allowed $\bar{x}_{\rm H\,II}$ values ($\bar{x}_{\rm H\,II} > 72$ per cent at $z = 9.1$) is inconsistent with other probes of reionization and would be ruled out if joined constraints were considered: e.g. Ly α damping wing absorption in the spectrum of the quasar at $z = 7.54$ suggests that the Universe is ~ 60 per cent neutral at that redshift (ionization fraction less than 40 per cent, Bañados et al. 2018; Davies et al. 2018). The quantitative joint analysis, however, is beyond the scope of this paper.

5.4 The optimal exclusion space

In the analysis above, we considered two separate data sets: the model parameters with $\vec{\theta} = [f_*,\ V_c,\ f_X,\ \tau,\ R_{\rm mfp},\ A_{\rm r}]$ and the derived IGM parameters with $\vec{\theta} = [T_{\rm gas},\ \bar{x}_{\rm H\,II},\ z_{\rm re},\ \Delta z]$. We showed that LOFAR is most sensitive to the radio background amplitude and to the thermal history of the IGM. To strengthen this point here, we focus our attention on just these two parameters, i.e. $A_{\rm r}$ and $T_{\rm gas}$. These parameters are independent as the gas temperature is determined by properties of astrophysical sources (mainly V_c, f_*, and f_X), while $A_{\rm r}$ is the amplitude of the phenomenological radio background.

We calculate the normalized probability for $A_{\rm r}$ and $T_{\rm gas}$ marginalizing over V_c, f_*, and f_X. For simplicity, we fix the reionization parameters $R_{\rm mfp} = 40$ comoving Mpc and $\tau = 0.055$. We show the resulting 2D and 1D probabilities in Fig. 7. As a sanity check, we calculate 68 per cent (grey), 95 per cent (black), and 99 per cent (not shown) confidence intervals finding that, at 95 per cent confidence level, LOFAR data rule out $A_{\rm r} > 182$ and $T_{\rm gas} < 2.89$ K at $z = 9.1$ and at 99 per cent LOFAR data rule out $A_{\rm r} > 259$ and $T_{\rm gas} < 2.25$ K. These limits are consistent with our previous numbers in Table 2.

6 QUALITATIVE COMPARISON WITH PREVIOUS RESULTS

Ghara et al. (2020) explored the implications of the LOFAR data in terms of the astrophysical parameter and statistical constraints on the IGM properties assuming standard-physics models (with the CMB as the background radiation). We verify the consistency of our conclusions with Ghara et al. (2020) by qualitatively comparing our standard case results for the thermal and ionization states of the IGM. A quantitative comparison between the two works is not possible at this stage because of the different choices of modelling, parametrization, and priors. Moreover, because the 21-cm signal is sensitive to the thermal and ionization histories the values of the gas temperature and ionization fraction can be directly constrained using the data. However, the mapping between these quantities and the astrophysical properties of the UV and X-ray sources (in our case f_*, V_c, f_X, τ, and $R_{\rm mfp}$) is model-dependent. Therefore, in this paper we refrain from comparing the astrophysical constraints leaving it for future work.

In their work, Ghara et al. (2020) explored two scenarios: (1) homogeneous spin temperature, which implies saturated Ly α background and homogeneous X-ray heating. The parameters that are varied in this case include gas temperature (or, equivalently, spin temperature), minimum halo mass and ionizing efficiency. (2) Inhomogeneous heating by soft X-ray sources with power-law SED where $M_{\rm min}$ and the spectral index of X-ray sources were kept fixed; the parameters that were varied are ionizing efficiency, X-ray efficiency (defined differently than in our work), and minimum mass of X-ray emitting haloes. In all cases, the value of star formation efficiency was kept fixed at $f_* = 2$ per cent. In comparison, we explore the popular case of heating by a realistic population of X-ray binaries with hard SED. In this case, heating is inefficient and fluctuations are smoothed out (Fialkov et al. 2014). Therefore, we expect our results to be closer to case (1) of Ghara et al. (2020). Moreover, in our work all the parameters (except for X-ray SED) are allowed to vary over a wide range, e.g. f_* is varied between 0.1 per cent and 50 per cent.

Despite these differences in modelling, qualitatively our work is consistent with Ghara et al. (2020). Both works rule out a cold IGM with an ionization fraction close to 50 per cent at $z = 9.1$. Namely, in their case (1) $\bar{x}_{\rm H\,II} \sim 0.24$–$0.6$ and $T_{\rm gas} \lesssim 3$ K are disfavoured (at 95 per cent), while we find that $\bar{x}_{\rm H\,II} \sim 0.38$–$0.72$ and $T_{\rm gas} \lesssim 10.1$ K are disfavoured (at 68 per cent).

7 CONCLUSIONS

In this paper, we have used the upper limit on the 21-cm signal from $z = 9.1$ based on 141 h of observations with LOFAR (Mertens et al. 2020) to evaluate the contribution of the high-redshift Universe to the excess radio background over the CMB detected by ARCADE2 (Fixsen et al. 2011) and LWA1 (Dowell & Taylor 2018). Assuming synchrotron spectrum of the radio background with spectral index $\beta = -2.6$ and marginalizing over the astrophysical properties of star-forming sources, we find (at 95 per cent CL) the contribution above the CMB level to be less than a factor of 182 at the reference frequency of 78 MHz, equivalent to 9.6 per cent of the CMB at 1.42 GHz. This limit, for the first time, rules out strong contribution of the high-redshift Universe to the excess detected by ARCADE2 and LWA1. At the level below 9.6 per cent of the CMB, the extra radio background could, on one hand, be strong enough to explain the tentative EDGES low-band detection that requires an excess of at least 0.1 per cent of the CMB (Fialkov & Barkana 2019). On the other

hand, such a small contribution would be within the measurement error (at 2σ level) of the LWA1 radio telescope. Hence, it would remain a plausible explanation for the detected EDGES signal, even if the excess radio background measured by ARCADE2 and LWA1 is due to an erroneous Galactic modelling (Subrahmanyan & Cowsik 2013).

We also use LOFAR data to constrain thermal and ionization state of the IGM at $z = 9.1$ in models with and without the extra radio background over the CMB. If such an extra radio background is present at $z = 9.1$, the fluctuations in the 21-cm signal are boosted compared to the standard case, which gives LOFAR a larger lever to reject models. Therefore, for the models with excess radio background, constraints on the astrophysical properties and the properties of the IGM are tighter than in the standard case. In particular, compared to the upper limit of 10.1 K (at 68 per cent CL) in the standard case, warmer IGM scenarios with mean neutral gas temperature of up to 16.1 K are disfavoured in the extra radio background models. In the latter case, we were also able to derive 95 per cent and 99 per cent CL on temperature of 2.89 and 2.25 K, respectively. Thus, the LOFAR data rule out the cold IGM scenarios in which the gas is expected to have a temperature of 2.1 K at $z = 9.1$ with 99.8 per cent CL.

Using the LOFAR data, we have also derived 68 per cent CL limits on the astrophysical parameters of Cosmic Dawn and EoR. The data disfavour very efficient star formation above 5 per cent, imply the existence of small haloes at early times (of masses below few$\times 10^8$ $M_\odot$ at $z = 9.1$), require the presence of X-ray sources, and disfavour a CMB optical depth above $\tau \sim 0.076$. For the suite of standard models, we point out that the LOFAR data rule out similar type of models as those rejected by the global signal experiments, namely the EDGES high-band (Monsalve et al. 2019) and SARAS2 (Singh et al. 2018). Finally, we note that our constraints of the standard-physics parameters are in a qualitative agreement with the results reported by Ghara et al. (2020). A detailed comparison between these two works is beyond the scope of this paper.

Although other high-redshift probes (e.g. the *Planck* measurement of the CMB optical, high-redshift quasars and galaxies) allow to put tighter constraints on the ionization history and properties of the UV sources at EoR, the 21-cm observations provide a unique way to probe the thermal history of the Universe and test the nature of the radio background. Because quantities such as temperature and ionization fraction at the LOFAR redshift $z = 9.1$ are the results of cumulative (rather than an instantaneous) effect of star formation over the entire cosmic history, in this work we have refrained from using low-redshift constraints. Although the low-redshift observations constrain properties of bright galaxies during the EoR, they might be very different from the properties of high-redshift sources owing to the redshift evolution of stellar population (e.g. as a result of the gradual process of metal enrichment).

ACKNOWLEDGEMENTS

This work was supported by the Science and Technology Facilities Council (grant nos ST/F002858/1 and ST/I000976/1) and the South-east Physics Network (SEPNet). We acknowledge the usage of the DiRAC HPC. We also acknowledge that the results in this paper have been achieved using the PRACE Research Infrastructure resources Curie based at the Très Grand Centre de Calcul (TGCC) operated by CEA near Paris, France, and Marenostrum based in the Barcelona Supercomputing Center, Spain. Time on these resources was awarded by PRACE under PRACE4LOFAR grant nos 2012061089 and 2014102339 as well as under the Multiscale Reionization grant nos 2014102281 and 2015122822. The authors gratefully acknowledge the Gauss Centre for Supercomputing e.V. (www.gauss-centre.eu) for funding this project by providing computing time through the John von Neumann Institute for Computing (NIC) on the GCS Supercomputer JUWELS at Jülich Supercomputing Centre (JSC). AF is supported by the Royal Society University Research Fellowship. Some of the numerical computations were done on the Apollo cluster at The University of Sussex. This project/publication was made possible for RB through the support of a grant from the John Templeton Foundation, as well as the ISF–NSFC joint research programme (grant no. 2580/17). The opinions expressed in this publication are those of the authors and do not necessarily reflect the views of the John Templeton Foundation.

DATA AVAILABILITY

The data underlying this article will be shared on a reasonable request to the corresponding author.

REFERENCES

Bañados E. et al., 2018, Nature, 553, 473
Barkana R., 2016, Phys. Rep., 645, 1
Barkana R., 2018a, The Encyclopedia of Cosmology. Volume 1: Galaxy Formation and Evolution Rennan Barkana. Tel Aviv University, Israel
Barkana R., 2018b, Nature, 555, 71
Barkana R., Loeb A., 2001, Phys. Rep., 349, 125
Barry N. et al., 2019, ApJ, 884, 1
Beardsley A. P. et al., 2016, ApJ, 833, 102
Behroozi P., Wechsler R. H., Hearin A. P., Conroy C., 2019, MNRAS, 488, 3143
Bernardi G. et al., 2016, MNRAS, 461, 2847
Bharadwaj S., Pandey S. K., 2005, MNRAS, 358, 968
Biermann P. L., Nath B. B., Caramete L. I., Harms B. C., Stanev T., Becker Tjus J., 2014, MNRAS, 441, 1147
Bowman J. D., Rogers A. E. E., Monsalve R. A.,Mozdzen T. J., Mahesh N. , 2018, Nature, 555, 67
Bradley R. F., Tauscher K., Rapetti D., Burns J. O., 2019, ApJ, 874, 153
Brandenberger R., Cyr B., Schaeffer T., 2019, J. Cosmol. Astroparticle Phys., 2019, 020
Cappelluti N. et al., 2012, MNRAS, 427, 651
Chianese M., Di Bari P., Farrag K., Samanta R., 2018, preprint (arXiv:1805.11717)
Chuzhoy L., Shapiro P. R., 2007, ApJ, 655, 843
Cohen A., Fialkov A., Barkana R., 2016, MNRAS, 459, L90
Cohen A., Fialkov A., Barkana R., Lotem M., 2017, MNRAS, 472, 1915
Cohen A., Fialkov A., Barkana R., 2018, MNRAS, 478, 2193
Cohen A., Fialkov A., Barkana R., Monsalve R., 2019, preprint (arXiv:1910.06274)
Cohen A., Fialkov A., Barkana R., Monsalve R. A., 2020, MNRAS, 495, 4845
Dalal N., Pen U.-L., Seljak U., 2010, J. Cosmol. Astroparticle Phys., 2010, 007
Davies F. B. et al., 2018, ApJ, 864, 142
Dowell J., Taylor G. B., 2018, ApJ, 858, L9
Eastwood M. W. et al., 2019, AJ, 158, 84
Ewall-Wice A., Chang T. C., Lazio J., Doré O., Seiffert M., Monsalve R. A., 2018, ApJ, 868, 63
Ewall-Wice A., Chang T.-C., Lazio T. J. W., 2019, MNRAS, 492, 6086
Feng C., Holder G., 2018, ApJ, 858, L17
Fialkov A., Barkana R., 2014, MNRAS, 445, 213
Fialkov A., Barkana R., 2019, MNRAS, 486, 1763
Fialkov A., Barkana R., Visbal E., Tseliakhovich D., Hirata C. M., 2013, MNRAS, 432, 2909
Fialkov A., Barkana R., Visbal E., 2014, Nature, 506, 197
Fialkov A., Cohen A., Barkana R., Silk J., 2017, MNRAS, 464, 3498
Field G. B., 1958, Proc. IRE, 46, 240
Fixsen D. J. et al., 2011, ApJ, 734, 5
Fling C., 2019, University of Sussex, UK

Fragos T. et al., 2013, ApJ, 764, 41
Fraser S. et al., 2018, Phys. Lett. B, 785, 159
Furlanetto S. R., Zaldarriaga M., Hernquist L., 2004, ApJ, 613, 16
Furlanetto S. R., Oh S. P., Briggs F. H., 2006, Phys. Rep., 433, 181
Gehlot B. K. et al., 2019, MNRAS, 488, 4271
Ghara R., Mellema G., 2019, MNRAS, 492, 634
Ghara R. et al., 2020, MNRAS, 493, 4728
Greig B., Mesinger A., Pober J. C., 2016, MNRAS, 455, 4295
Greig B., Mesinger A., Haiman Z., Simcoe R. A., 2017, MNRAS, 466, 4239
Greig B., Mesinger A., Bañados E., 2019, MNRAS, 484, 5094
Haiman Z., Rees M. J., Loeb A., 1997, ApJ, 476, 458
Hills R., Kulkarni G., Meerburg P. D., Puchwein E., 2018, Nature, 564, E32
Jana R., Nath B. B., Biermann P. L., 2019, MNRAS, 483, 5329
Jennings W. D., Watkinson C. A., Abdalla F. B., McEwen J. D., 2019, MNRAS, 483, 2907
Kern N. S., Liu A., Parsons A. R., Mesinger A., Greig B., 2017, ApJ, 848, 23
Kolopanis M. et al., 2019, ApJ, 883, 133
Lehmer B. D., Alexander D. M., Bauer F. E., Brandt W. N., Goulding A. D., Jenkins L. P., Ptak A., Roberts T. P., 2010, ApJ, 724, 559
Lehmer B. D. et al., 2012, ApJ, 752, 46
Li W. et al., 2019, ApJ, 887, 141
Maio U., Koopmans L. V. E., Ciardi B., 2011, MNRAS, 412, L40
Mason C. A., Treu T., Dijkstra M., Mesinger A., Trenti M., Pentericci L., de Barros S., Vanzella E., 2018, ApJ, 856, 2
Mellema G., Iliev I. T., Pen U.-L., Shapiro P. R., 2006, MNRAS, 372, 679
Mertens F. G. et al., 2020, MNRAS, 493, 1662
Mesinger A., 2019, The Cosmic 21-cm Revolution; Charting the First Billion Years of Our Universe, Institute of Physics Publishing
Mesinger A., Furlanetto S., Cen R., 2011, MNRAS, 411, 955
Mineo S., Gilfanov M., Sunyaev R., 2012, MNRAS, 419, 2095
Mirocha J., Furlanetto S. R., 2019, MNRAS, 483, 1980
Mondal R., Bharadwaj S., Majumdar S., Bera A., Acharyya A., 2015, MNRAS, 449, L41
Mondal R., Bharadwaj S., Majumdar S., 2016, MNRAS, 456, 1936
Mondal R., Bharadwaj S., Majumdar S., 2017, MNRAS, 464, 2992
Monsalve R. A., Rogers A. E. E., Bowman J. D., Mozdzen T. J., 2017, ApJ, 847, 64
Monsalve R. A., Greig B., Bowman J. D., Mesinger A., Rogers A. E. E., Mozdzen T. J., Kern N. S., Mahesh N., 2018, ApJ, 863, 11
Monsalve R. A., Fialkov A., Bowman J. D., Rogers A. E. E., Mozdzen T. J., Cohen A., Barkana R., Mahesh N., 2019, ApJ, 875, 67
O'Shea B. W., Wise J. H., Xu H., Norman M. L., 2015, ApJ, 807, L12
Paciga G. et al., 2013, MNRAS, 433, 639
Patil A. H. et al., 2017, ApJ, 838, 65
Planck Collaboration et al., 2014, A&A, 571, A16
Planck Collaboration et al., 2018, preprint (arXiv:1807.06209)
Pober J. C. et al., 2014, ApJ, 782, 66
Pospelov M., Pradler J., Ruderman J. T., Urbano A., 2018, Phys. Rev. Lett., 121, 031103
Price D. C. et al., 2018, MNRAS, 478, 4193
Schauer A. T. P., Liu B., Bromm V., 2019, ApJ, 877, L5
Sharma P., 2018, MNRAS, 481, L6
Sims P. H., Pober J. C., 2019, MNRAS, 492, 22
Singh S., Subrahmanyan R., 2019, ApJ, 880, 26
Singh S. et al., 2017, ApJ, 845, L12
Singh S. et al., 2018, ApJ, 858, 54
Sobacchi E., Mesinger A., 2013, MNRAS, 432, 3340
Spinelli M., Bernardi G., Santos M. G., 2019, MNRAS, 489, 4007
Subrahmanyan R., Cowsik R., 2013, ApJ, 776, 42
Sullivan D., Iliev I. T., Dixon K. L., 2018, MNRAS, 473, 38
Trott C. M. et al., 2020, MNRAS, preprint (arXiv:2002.02575)
Tseliakhovich D., Hirata C., 2010, Phys. Rev. D, 82, 083520
Venumadhav T., Dai L., Kaurov A., Zaldarriaga M., 2018, Phys. Rev. D, 98, 103513
Visbal E., Barkana R., Fialkov A., Tseliakhovich D., Hirata C. M., 2012, Nature, 487, 70
Weinberger L. H., Haehnelt M. G., Kulkarni G., 2019, MNRAS, 485, 1350
Wise J. H., Demchenko V. G., Halicek M. T., Norman M. L., Turk M. J., Abel T., Smith B. D., 2014, MNRAS, 442, 2560
Wouthuysen S. A., 1952, AJ, 57, 31
Xu H., Wise J. H., Norman M. L., Ahn K., O'Shea B. W., 2016, ApJ, 833, 84

APPENDIX: ARTIFICIAL NEURAL NETWORKS

Both numerical and seminumerical simulations are too slow and computationally expensive to sample the 21-cm signal parameter space effectively. Jennings et al. (2019) evaluated the performance of five machine-learning algorithms, and found deep ANN to be the most efficient and best performing model to predict the 21-cm power spectra.

In order to produce a data set large enough to perform the statistical analysis outlined in Section 4, we use an emulator for the 21-cm power spectra based on an ANN (see Fling 2019 for more details on methodology). This allows us to sample the parameter space more thoroughly than the simulations permit and produce the large ensemble of models necessary for our analysis. The network was trained on the seminumerical simulations for both the excess-background and standard cases described in Section 3, then used to predict the binned spherically averaged power spectra and sample variances (Section 3.1) at $z = 9.1$ in all seven LOFAR k-bins (see Table 1).

Our neural network was built with the PYTHON package Keras,[12] which runs on top of Tensorflow.[13] The network consists of four hidden layers of sizes, 300, 300, 300, and 10, respectively. We trained the network with data sets of size 7702 and 16 270 for the excess-background and standard cases, respectively. Note that these data sets are slightly larger than the ones reported in Section 3 because they include parameters with values outside the prior ranges specified in Section 3. In particular, we include lower and higher values of τ (between 0.022 and 0.11), higher values of f_X (up to 1000), and higher values of A_r (up to ∼200 per cent of the CMB at 1.42 GHz). These extreme models help to train ANN but are not used in the likelihood calculations. To prevent over fitting, we validated the network with 25 per cent of the total models.

In total, we have used four different emulators that are listed in Table A1. Fig. A1 shows the excess background emulator accuracy for four k-bins. The accuracy of the emulators is quantified through root-mean-square error ($\sigma_{\rm ann}$). Although the plot shows ∼ 20 per cent scatter, we have checked that $\sigma_{\rm ann}$ is smaller than 10 per cent, which is our floor on the theoretical uncertainty, $\sigma_{\rm th}(k_c)$. We have also checked the effects of modelling uncertainty on our limits and confirm that the results are mainly dominated by the measurement errors. The effect of the uncertainty in theory and ANN are sub-dominant. In particular, taking the theoretical+ANN error to be 30 per cent does not change the result. The ANN were used to populate the parameter space described in Section 3. These emulated models are combined with the original set to comprise the data used for our likelihood analysis.

[12] https://keras.io
[13] https://www.tensorflow.org

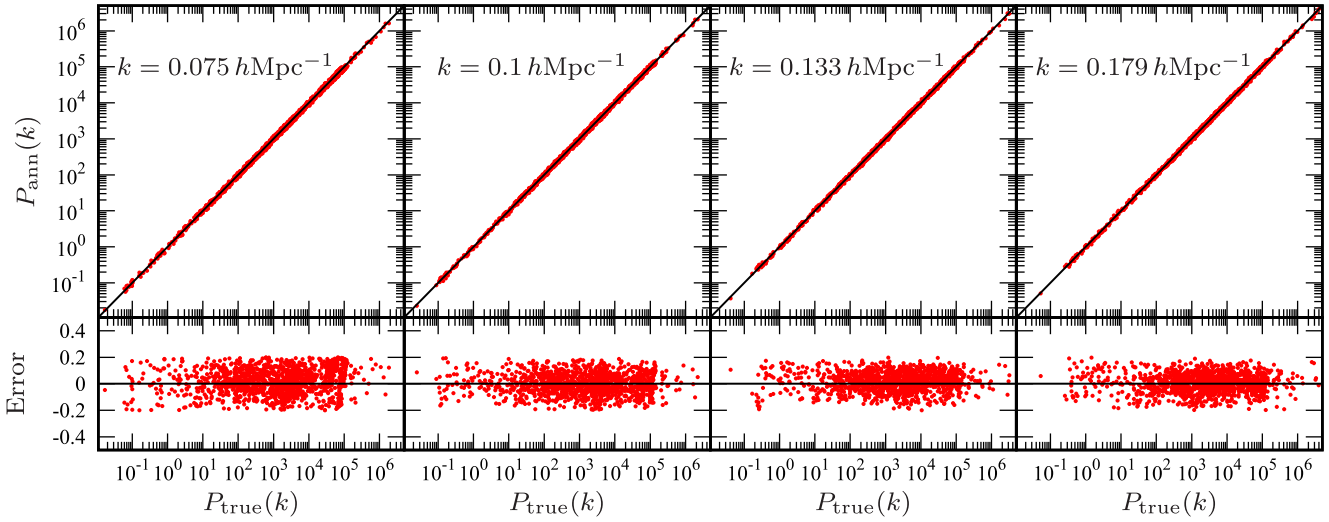

Figure A1. The binned power-spectrum values computed by the ANN emulator against the true values used for validation for the excess-background models. We show results only for four k-bins mentioned in the figure. The bottom panels show the relative difference. Note that the rms error (Table A1) is calculated using data from all the seven k-bins.

Table A1. Specifications of different emulators used in our analysis.

Model	Number neurons in the input layer	Parameters used in the input layers	Number neurons in the output layer	rms error $\sigma_{\rm ann}$ (per cent)	Result
Excess-background	6	$[f_*,\ V_c,\ f_X,\ \tau,\ R_{\rm mfp},\ A_{\rm r}]$	14	7.2	Fig. 3
Standard	5	$[f_*,\ V_c,\ f_X,\ \tau,\ R_{\rm mfp}]$	14	6.4	Fig. 5
Excess-background	4	$[T_{\rm gas},\ \bar{x}_{\rm H\,II},\ z_{\rm re},\ \Delta z]$	14	5	Fig. 6 (left)
Standard	4	$[T_{\rm gas},\ \bar{x}_{\rm H\,II},\ z_{\rm re},\ \Delta z]$	14	4	Fig. 6 (right)

This paper has been typeset from a TEX/LATEX file prepared by the author.